LETTERS
https://doi.org/10.1038/s41550-020-1142-z

nature astronomy

Check for updates

An ultrahot Neptune in the Neptune desert

James S. Jenkins[1,2]✉, Matías R. Díaz[1,2], Nicolás T. Kurtovic[1], Néstor Espinoza[3], Jose I. Vines[1], Pablo A. Peña Rojas[1], Rafael Brahm[4,5,40], Pascal Torres[4], Pía Cortés-Zuleta[1], Maritza G. Soto[6], Eric D. Lopez[7], George W. King[8,9], Peter J. Wheatley[8,9], Joshua N. Winn[10], David R. Ciardi[11], George Ricker[12], Roland Vanderspek[13], David W. Latham[14], Sara Seager[12,15], Jon M. Jenkins[16], Charles A. Beichman[11], Allyson Bieryla[14], Christopher J. Burke[12], Jessie L. Christiansen[11], Christopher E. Henze[16], Todd C. Klaus[16], Sean McCauliff[16], Mayuko Mori[17], Norio Narita[18,19,20,21,22], Taku Nishiumi[23], Motohide Tamura[17,20,21], Jerome Pitogo de Leon[17], Samuel N. Quinn[14], Jesus Noel Villaseñor[12], Michael Vezie[12], Jack J. Lissauer[16], Karen A. Collins[14], Kevin I. Collins[24], Giovanni Isopi[25], Franco Mallia[25], Andrea Ercolino[25], Cristobal Petrovich[26,27], Andrés Jordán[5,28], Jack S. Acton[29], David J. Armstrong[8,9], Daniel Bayliss[8], François Bouchy[30], Claudia Belardi[29], Edward M. Bryant[8,9], Matthew R. Burleigh[29], Juan Cabrera[31], Sarah L. Casewell[29], Alexander Chaushev[32], Benjamin F. Cooke[8,9], Philipp Eigmüller[31], Anders Erikson[31], Emma Foxell[8,9], Boris T. Gänsicke[8], Samuel Gill[8,9], Edward Gillen[33], Maximilian N. Günther[12], Michael R. Goad[29], Matthew J. Hooton[34], James A. G. Jackman[8,9], Tom Louden[8,9], James McCormac[8,9], Maximiliano Moyano[35], Louise D. Nielsen[30], Don Pollacco[8,9], Didier Queloz[33], Heike Rauer[31,32,36], Liam Raynard[29], Alexis M. S. Smith[31], Rosanna H. Tilbrook[29], Ruth Titz-Weider[31], Oliver Turner[30], Stéphane Udry[30], Simon. R. Walker[8], Christopher A. Watson[34], Richard G. West[8,9], Enric Palle[22,37], Carl Ziegler[38], Nicholas Law[39] and Andrew W. Mann[39]

About 1 out of 200 Sun-like stars has a planet with an orbital period shorter than one day: an ultrashort-period planet[1,2]. All of the previously known ultrashort-period planets are either hot Jupiters, with sizes above 10 Earth radii ($R_\oplus$), or apparently rocky planets smaller than 2 $R_\oplus$. Such lack of planets of intermediate size (the 'hot Neptune desert') has been interpreted as the inability of low-mass planets to retain any hydrogen/helium (H/He) envelope in the face of strong stellar irradiation. Here we report the discovery of an ultrashort-period planet with a radius of 4.6 $R_\oplus$ and a mass of 29 $M_\oplus$, firmly in the hot Neptune desert. Data from the Transiting Exoplanet Survey Satellite[3] revealed transits of the bright Sun-like star LTT 9779 every 0.79 days. The planet's mean density is similar to that of Neptune, and according to thermal evolution models, it has a H/He-rich envelope constituting $9.0^{+2.7}_{-2.9}$% of the total mass. With an equilibrium temperature around 2,000 K, it is unclear how this 'ultrahot Neptune' managed to retain such an envelope. Follow-up observations of the planet's atmosphere to better understand its origin and physical nature will be facilitated by the star's brightness ($V_{mag} = 9.8$).

Using high-precision photometry from Sector 2 of the Transiting Exoplanet Survey Satellite (TESS) mission at a cadence of 2 min, a candidate transiting planet was flagged for the star LTT 9779[4]. The candidate was released as a TESS alert in October 2018, and assigned the TESS object of interest (TOI) tagname TOI-193 (TIC 183985250). The TESS lightcurve was scrutinized before its public release. No transit-depth variations were apparent, no motion of the stellar image was detected during transits and no secondary eclipses could be found. Data from the Gaia spacecraft[5,6] revealed only one background star within the TESS photometric aperture, but it is 5 mag fainter than LTT 9779 and hence cannot be the source of the transit-like signals, and no notable excess scatter was witnessed in the Gaia measurements. The lack of all these abnormalities supported the initial interpretation that the transit signals are due to a planet with an orbital period of 19 h and a radius of 3.96 $R_\oplus$.

We also observed four complete transits with ground-based facilities: three with the Las Cumbres Observatory (LCO) and one with the Next Generation Transit Survey (NGTS[7]) telescopes. The LCO and NGTS data have a similar precision to the TESS lightcurve and much better angular resolution. The observed transit depths were in agreement with the depth observed with TESS. High-angular resolution imaging of LTT 9779 was performed with adaptive optics using the Near InfraRed Camera 2 (NIRC2) at the Keck Observatory, and with speckle imaging in the optical using the high-resolution camera (HRCam) on the Southern Astrophysical Research (SOAR) telescope at the Cerro-Tololo Inter-American Observatory. No companions were detected within a radius of 3″ down to a contrast level of 7.5 mag, and no bright close binary was seen with a resolution of 0.05″ (Methods). These observations sharply reduce the possibility that an unresolved background star is the source of the transits. We also tested the probability of having background or foreground stars within a region of 0.1″ separation

A full list of affiliations appears at the end of the paper.

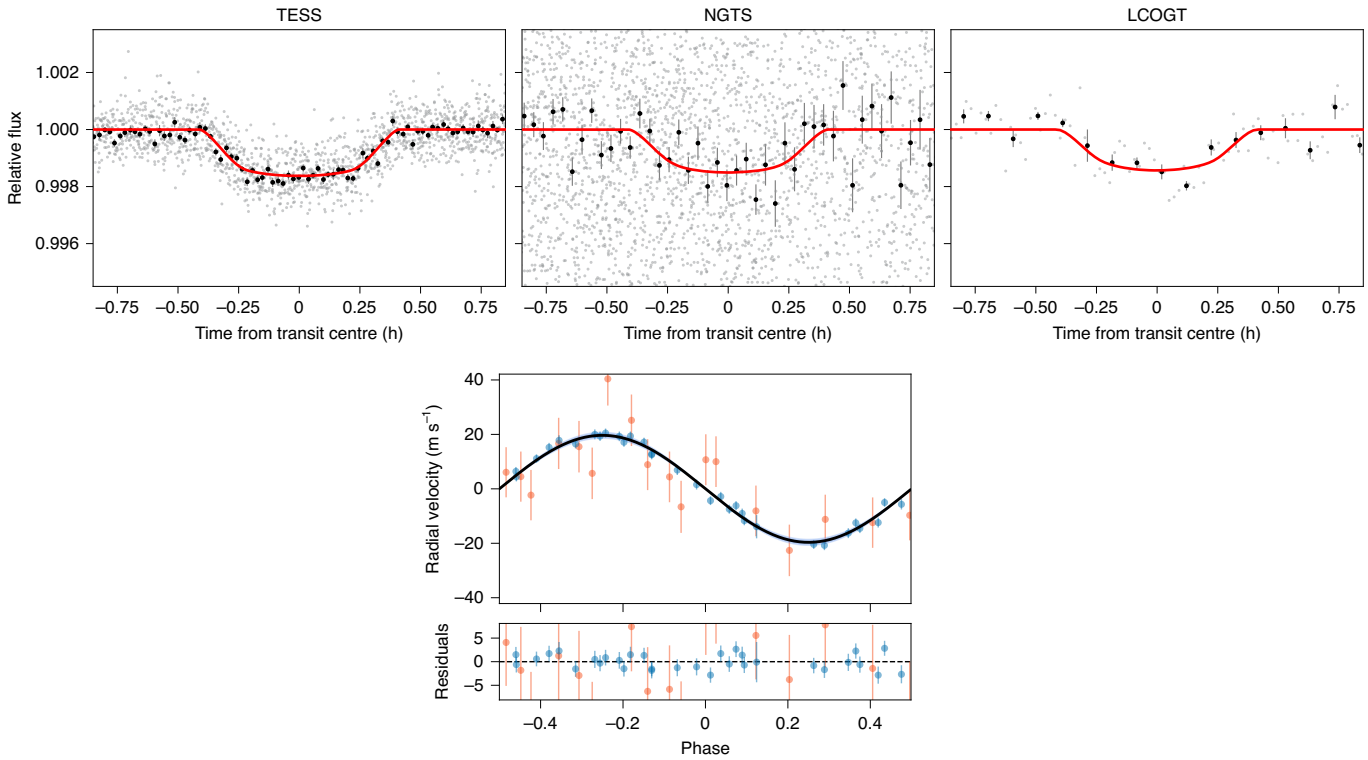

Fig. 1 | Transit lightcurves and phase-folded radial velocities for LTT 9779. Top: the discovery TESS lightcurve averaged over 33 transits (left) and the single transit follow-up photometry from the NGTS (middle) and LCOGT (right) for LTT 9779, with a 0.8 d period, and including the associated transit model using the parameters shown in Table 1. The full dataset is shown by the small points and the binned data are superimposed on these as the larger and darker points with associated uncertainties. Bottom: the 31 HARPS radial velocities in blue and 18 Coralie measurements in orange (Supplementary Table 2), also folded to the period of the planet, and with their respective uncertainties. The mean uncertainty of the Coralie velocities is a factor of ten larger than those from HARPS. The best-fit model is again overplotted on the data. The TESS, NGTS and LCOGT photometry, along with the HARPS and Coralie velocities, were fit simultaneously to ensure the best constraints possible on the planet parameters, along with a more accurate description of the overall uncertainties.

(adaptive optics limit) from the star, using a Besançon[8] model of the galaxy. The model indicates we can expect over 2,200 stars in a 1 square degree field around LTT 9779 providing a probability of only 0.0005% of having a star down to a magnitude limit of $V=21$ contaminating the lightcurves. If we consider only objects bright enough to cause contamination of the transit depth that would substantially alter the planet properties, this probability drops even more (see Methods for more details). Furthermore, although there is a 13.5% probability that LTT 9779 could be part of a binary system that passes within this separation limit, spectral analysis rules out all allowable masses whose contaminant light that would be required to push LTT 9779 b outside of the Neptune desert.

Final confirmation of the planet's existence came from high-cadence radial-velocity observations with the High Accuracy Radial-velocity Planet Searcher (HARPS[9]). A sinusoidal radial-velocity signal was detected with the EMPEROR code (P. A. Peña-Rojas and J. S. Jenkins, manuscript in preparation) independently of the transit data, but with a matching orbital period and phase. No other notable signals were detected, nor were any longer-term trends, ruling out additional massive planets with orbital periods of a few years or less. Likewise, no transit timing variations were detected (Methods).

To determine the stellar properties, we combined the Gaia data with spectral information from HARPS, along with other spectra from the Tillinghast Reflector Echelle Spectrograph (TRES[10]) and the Network of Robotic Echelle Spectrographs (NRES[11]) and compared the star's observable properties to the outputs from theoretical stellar-evolutionary models (MESA Isochrones and Stellar Tracks (MIST) and Yonsei–Yale). We also used our new ARIADNE code to precisely calculate the effective temperature and stellar radius (see Methods for more information on these methods). The star was found to have a mass, radius and age to 1σ of $1.02^{+0.02}_{-0.03}\,M_{\odot}$, $0.949\pm0.006\,R_{\odot}$ and $2.0^{+1.3}_{-0.9}$ Gyr, respectively. The effective temperature and surface gravity are consistent with a main-sequence star slightly cooler than the Sun. The spectra also revealed the star to be approximately twice as metal rich as the Sun ($[\mathrm{Fe/H}]=+0.25\pm0.04$ dex). Supplementary Table 1 displays all the parameter values.

We utilized the juliet code[12] to perform a joint analysis of the transit and radial-velocity data (Fig. 1). The period, mass and radius of the planet were found to be 0.792054 ± 0.000014 d, $29.32^{+0.78}_{-0.81}\,M_{\oplus}$ and $4.72\pm0.23\,R_{\oplus}$, respectively. The orbit is circular to within the limits allowed by the radial-velocity data (the posterior odds ratio is 49:1 in favour of a circular model over an eccentric model).

LTT 9779 b sits in the hot Neptune desert[13] (Fig. 2), providing an opportunity to study the link between short-period gas giants and lower-mass super-Earths. The planet's mean density is similar to that of Neptune, and the planet's mass and radius are incompatible with either a pure rock or pure water composition (Fig. 3), implying that it possesses a substantial H/He gaseous atmosphere. Using one-dimensional thermal evolution models from ref. [14], assuming a silicate and iron core and a solar composition gaseous envelope, we find a planet core mass of $27.9^{+1.2}_{-1.0}\,M_{\oplus}$, and an atmospheric mass

Table 1 | Transit, orbital and physical parameters of LTT 9779 b

Parameter	Prior	Value
Lightcurve parameters		
P (d)	$N(0.792, 0.1)$	0.7920520 ± 0.0000093
T_0 (d)	$N(2{,}458{,}354.22, 0.1)$	$2{,}458{,}354.21430 \pm 0.00025$
r_1	$U(0, 1)$	$0.9417^{+0.0048}_{-0.0060}$
r_2	$U(0, 1)$	$0.0454^{+0.0022}_{-0.0017}$
ρ_* (kg m^3)	$N(1{,}810, 130)$	$1,758^{+125}_{-121}$
$q_{1,\mathrm{TESS}}$	$U(0, 1)$	$0.45^{+0.20}_{-0.16}$
$q_{2,\mathrm{TESS}}$	$U(0, 1)$	$0.43^{+0.35}_{-0.30}$
$q_{1,\mathrm{NGTS}}$	$U(0, 1)$	$0.63^{+0.25}_{-0.32}$
$q_{2,\mathrm{NGTS}}$	$U(0, 1)$	$0.55^{+0.31}_{-0.35}$
Radial-velocity parameters		
K (m s^{-1})	$U(-100, 100)$	$19.65^{+0.43}_{-0.43}$
e	0	0
ω (°)	90	90
$\gamma_{\mathrm{Coralie}}$ (m s^{-1})	$N(0, 100)$	$-5.09^{+2.20}_{-2.20}$
γ_{HARPS} (m s^{-1})	$N(0, 100)$	$-4.40^{+0.30}_{-0.31}$
$\sigma_{\mathrm{Coralie}}$ (m s^{-1})	$J(10^{-2}, 100)$	$8.03^{+2.15}_{-1.74}$
σ_{HARPS} (m s^{-1})	$J(10^{-2}, 100)$	$1.43^{+0.28}_{-0.24}$
Derived parameters		
R_p/R_*	-	$0.0455^{+0.0022}_{-0.0017}$
a/R_*	-	$3.877^{+0.090}_{-0.091}$
i	-	76.39 ± 0.43
M_p ($M_\oplus$)	-	$29.32^{+0.78}_{-0.81} M_\oplus$
R_p ($R_\oplus$)	-	$4.72 \pm 0.23\ R_\oplus$
$\langle T_{\mathrm{eq}} \rangle$ (K)[a]	-	$1,978 \pm 19$
a (au)	-	$0.01679^{+0.00014}_{-0.00012}$
ρ_p (g cm^{-3})	-	1.536 ± 0.123

For the prior descriptions, which are the expected probability distributions for each of the fit parameters, $N(\mu, \sigma)$ represents a normal distribution with mean μ and standard deviation σ, whereas $U(a, b)$ and $J(a, b)$ represent a uniform prior and Jeffrey's prior, both defined between points a and b, respectively (see 'Global modelling' in Methods for more information). T_0 represents the calculated center of transit time, ρ_* is the stellar density, K is the radial velocity semi-amplitude, γ represents the mean radial velocity offset for the individual instruments, a is the semimajor axis of the planetary orbit, M_p is the planet mass, T_{eq} the equilibrium temperature of the planet, and ρ_p the calculated planet bulk density. [a]Equilibrium temperature using equation (4) of ref. [92] with $A = 0.4$, $\beta = 0.5$ and $\epsilon = 1$, where A is the planetary albedo, β is the fraction of the planet's surface that re-radiates the absorbed radiation, and ϵ represents the broadband thermal emissivity.

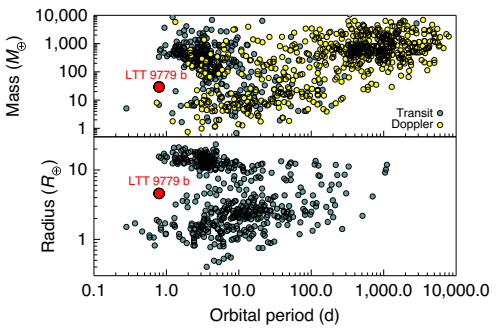

Fig. 2 | LTT 9779 b in the period–mass and period–radius planes. Top: all currently confirmed planets with a fractional mass uncertainty below 30%, separated in colour by their detection method. Bottom: all currently confirmed transit planets with a fractional radius uncertainty below 5%. LTT 9779 b is clearly isolated in the Neptune desert in period–mass–radius space, meaning it is heavily decoupled from the current populations of known exoplanets.

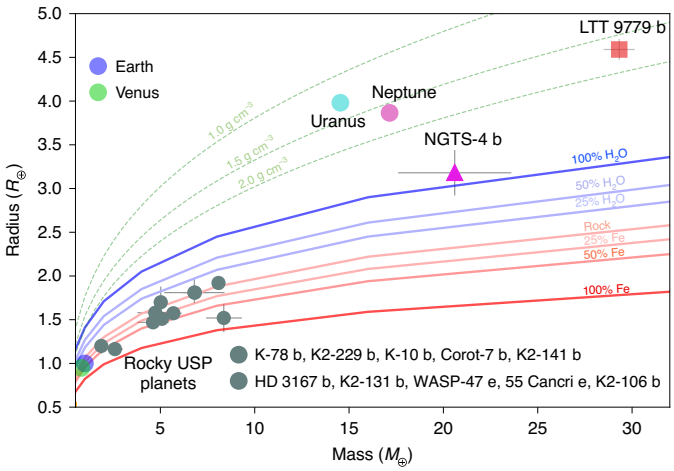

Fig. 3 | LTT 9779 b in the mass–radius plane. The plot includes all non-gas giant USPs with well constrained Doppler masses, and their associated published uncertainties. LTT 9779 b is marked by the red square. Structure models from ref. [93] are plotted as solid curves and labelled depending on the bulk composition of the planet. The models range from a 100% iron core planet to a 100% waterworld. The USPs all agree with rocky-iron compositions, explained by photoevaporation of their primordial atmospheres. LTT 9779 b is significantly larger, indicating that it has a residual hydrogen and helium atmosphere around the core. Dashed isodensity curves are shown in green for reference, highlighting the similar densities between Neptune and LTT 9779 b. For reference, Venus, Earth, Uranus and Neptune are represented in the plot.

fraction of $9.0^{+2.7}_{-2.9}$%. We also tested other planet structures, and even in the limiting case of a non-physical pure waterworld, there still exists a substantial H/He-rich envelope, at the level of $2.2^{+1.1}_{-1.6}$ %. When combined with the high equilibrium temperature for the planet of $1{,}978 \pm 19$ K, this makes LTT 9779 b an excellent target for future transmission spectroscopy, secondary eclipse studies and phase variation analyses. All of the planetary model parameters are in Table 1.

LTT 9779 b is the most highly irradiated Neptune-sized planet yet found. It is firmly in the region of parameter space known as the 'evaporation desert' where observations have shown a clear absence of similarly sized planets[1,15], and models of photo-evaporative atmospheric escape predict that such low-density gaseous atmospheres should be evaporated on short timescales[16,17]. As LTT 9779 b is a mature planet found in this desert, it is a particularly high-priority target for transmission spectroscopy at wavelengths that probe low-density material escaping from planetary upper atmospheres such as Lyman α[18], far-ultraviolet metal lines[19], Ca and Fe lines[20], and the 1.083 μm He line[21].

An interesting comparison can be made between LTT 9779 b and NGTS-4 b[22], the most similar of all the other known planets. NGTS-4 b is not as hot ($\langle T_{\mathrm{eq}} \rangle = 1,650 \pm 400$ K) or short period ($P = 1.337351 \pm 0.000008$ d) as LTT 9779 b, has a much higher density of 3.45 g cm^{-3} and orbits a metal-poor star ([M/H] = −0.28 ± 0.10 dex). These characteristics may be clues that the two planets formed differently: NGTS-4 b may have formed as a relatively small and dense world, whereas LTT 9779 b started life

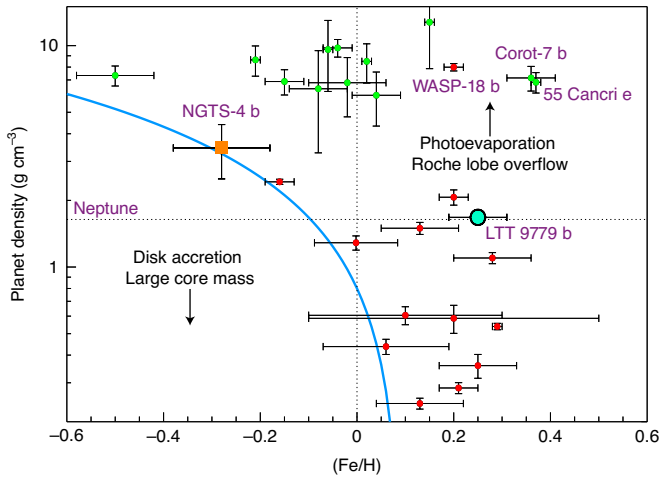

Fig. 4 | Distribution of planetary densities as a function of host-star metallicity for currently known transiting planets with orbital periods less than 1.3 d. The sample is split into those with masses less than 0.1 M_J (green circles; USP planet proxies) and those with masses above (red circles; Ultrahot Jupiter proxies), plotted with their published uncertainties. The ultrahot Neptune LTT 9779 b and longer period NGTS-4 b are clearly labelled in the figure. The blue curve is a power law described by $3.5\times[(N_{Fe}/N_H)/(N_{Fe}/N_H)_\odot]^{-2.5}+0.8$, where N relates to the number of associated atoms, which bounds the regions governed by the physical processes that determine the planet bulk properties. Those physical processes and the direction in which they move planets are shown in the plot.

as a much larger and less dense planet (Fig. 4). Indeed, photoevaporation models posit that the bulk population of ultrashort-period (USP) planets form by growing to around 3 $M_\oplus$, through the accretion of various amounts of light elements from the protoplanetary disk. The intense radiation from the young star then evaporates these close-in planets over an interval on the order of 10^8 yr, leaving behind small rocky planets with radii less than 1.5 $R_\oplus$ (ref. [17]). The more massive population of planets can hold onto the bulk of their envelopes until the star becomes quiescent, leaving behind planets with radii 2–3 $R_\oplus$. However, these planets are generally found to have orbital periods beyond 1 d, similar to NGTS-4 b, reaching out to 100 d or so. USP planets with these radii are rare, and it may be that since LTT 9779 b likely has a large mass, it can hold onto a high fraction of its atmosphere. It could also have migrated to its current position over a longer dynamical timescale, 10^9 yr, not leaving enough time to blow off a large fraction of its atmosphere by photoevaporation.

Assuming energy-limited atmospheric escape, and adopting the current mass, radius and orbital separation of LTT 9779 b, we estimate mass-loss rates of 2×10^{12}–8×10^{12} g s^{-1} during the saturated phase of X-ray emission (for efficiencies of 5–25% (refs. [23,24])). Assuming the X-ray evolution given by ref. [25] and the corresponding extreme-ultraviolet emission by refs. [26,27], we estimate a total mass loss of 2–9 $M_\oplus$. Considering instead the hydrodynamic calculations by ref. [28], this mass loss increases to be greater than the total mass of the planet, and employing the detailed atmospheric escape evolution model of ref. [16] suggests that the planet could have had an atmospheric mass fraction of up to ~60% of the total planet mass, or around half that of Saturn (~44 $M_\oplus$). This means that LTT 9779 b could not have formed in situ with properties close to those we measure here, ruling out such a model. Conversely, adopting an initial planet mass and radius equal to that of Jupiter, we estimate a mass loss of 5.5×10^{28} g over the current age of the system, which would be only ~3% of the total initial planet mass. Therefore, we can be sure that if the planet began as a Jupiter-mass gas giant, photoevaporation cannot be the sole mechanism that removed most of its atmosphere.

One possible mechanism for atmospheric loss is Roche lobe overflow (RLO[29]). Planets with masses of ~1 M_J orbiting solar-mass stars can fill their Roche lobes for orbital periods approaching 12 h. For progenitor hot Jupiters with large cores (~30 $M_\oplus$), the initial migration inwards to the RLO orbit is driven by tidal interaction with the host star. The migration can then reverse as mass is stripped from the planet at a rate of 10^{13}–10^{14} g s^{-1} and continues on for 1 Gyr or so, assuming the escaping material settles in an accretion disk around the star and transfers its angular momentum back to the planet. The planet can migrate outwards, reaching an orbital period of ~0.8 d, before inward migration can resume. Planets with smaller masses undergo later inward migration within the mass-loss phase. After the completion of RLO, these planets remain with an atmosphere in the region of 7–10%, in agreement with that of LTT 9779 b, (assuming the planet is not still currently undergoing RLO). Although these planets terminate with no atmosphere and an orbital period of only 0.3 d after 2.1 Gyr of evolution, commensurate with the current age of LTT 9779 b, less massive planets terminate with orbital periods longer than more massive ones, and their mass-loss period increases also. Although some of these models qualitatively fit the data observed for LTT 9779 b, more work is still required to provide a stronger, more realistic description of the formation history of this system. Finally, such a model is also dependent on the assumption that LTT 9779 b started life as a gas giant planet, which is plausible given the planet's large heavy element abundance, and the fact that metal-rich stars are more commonly found to host gas giant planets than more metal-poor stars[30].

Methods

TESS photometry treatment. TESS observed the star LTT 9779 (HIP 117883, TIC 183985250, TOI-193) using Camera 2 (CCD 4), between 23 August 2018 and 20 September 2018 UT (Julian date 2,458,354.11439–2,458,381.51846), part of the Sector 2 observing campaign. The short cadence time sampling of the data was set to 2 min, and data products were then processed on the ground using the Science Processing Operations Center (SPOC) pipeline package[4], a modified version of the Kepler mission pipeline[31–34]. SPOC delivers data validation reports to MIT. These reports document so-called threshold crossing events identified by the SPOC pipeline, namely dips that could conceivably be due to transiting planets. A team in the TESS Science Office then reviews the reports, including analogous reports from analysis of the full frame images using the Quick-Look Pipeline developed at MIT. There are many criteria that go into deciding whether a threshold crossing event is an instrumental artefact or false alarm (for example, due to a low signal-to-noise ratio (SNR)), or an astrophysical false positive due to eclipsing binaries contaminating the TESS photometry or otherwise masquerading as transiting planets. This is the so-called vetting process. Candidates that survive vetting are then assigned TOI numbers and announced to the public, for example, at the Mikulski Archive for Space Telescopes, and then work by the TESS Follow-up Observing Program Working Group (TFOP WG) begins, tracking down TOIs that are not planets but could not be rejected based on the information available to the vetting team. TOIs that survive the reconnaissance work of the TFOP WG can then move on to precision radial-velocity work. LTT 9779 b was released as a TESS alert on the 4 October 2018, and assigned the code TOI-193. As part of the alert process candidate vetting, the lightcurve modelling did not show any hints of abnormality, such that no transit-depth variations were apparent, no point spread function centroiding offsets were found and no secondary eclipses reported, giving rise to a bootstrap false alarm probability of 2×10^{-278}.

In Extended Data Fig. 1, we show the TESS pre-search data conditioning lightcurve for LTT 9779, after removal of points that were flagged as being affected by excess noise. Given the quiescent nature of the star, the photometric lightcurve is fairly flat across the full time series, with the small transits (1,584 ± 43 ppm) readily apparent to the eye. This simplified the modelling effort, giving rise to the small residual scatter shown in the figure.

Follow-up NGTS photometry. Photometric follow-up observations of a full transit of LTT 9779 b was obtained on 25 December 2018 UT using the NGTS at the European Southern Observatory (ESO)'s Paranal Observatory[7]. We used a new mode of operation in which nine of the twelve individual NGTS telescopes were used to simultaneously monitor LTT 9779[35]. We find that the photometric noise is uncorrelated between the nine telescopes, and therefore we improve the photometric precision by a factor of three compared with a single NGTS telescope. The observations were obtained in photometric conditions and at airmass <2.

A total of 6,502 images were obtained, each with an exposure time of 10 s using the custom NGTS filter (520–890 nm). The observations were taken with the telescope slightly defocused to avoid saturation. The telescope guiding was performed using the DONUTS auto-guiding algorithm[36], which resulted in an root mean square of the target location on the charge-coupled device of only 0.040 pix, or 0.2″. Due to this high precision of the auto-guiding, the use of flat fields during the reduction of the images was not required. Comparison stars were chosen manually and aperture photometry was performed on the images using a custom aperture photometry pipeline. The wide field-of-view provided by NGTS enabled the selection of a good number of suitable comparison stars, despite LTT 9779 being a relatively bright star. When combined, the resulting photometry showed the transit signal of TOI-193 with a depth and transit centre time consistent with the TESS photometry. The combined NGTS lightcurve has a precision of 170 ppm over a half hour timescale, which is a comparable to the TESS precision of 160 ppm over this timescale (for a single transit).

Dilution probability. Given the reality of the transit as 'on source', the issue of dilution of the lightcurve by a foreground or background star is considered in a probabilistic sense. In this case, we aim to test the probability of having a blended star so close to the star angularly on the sky that the adaptive optics observations would not have detected it. The adaptive optics sensitivity deteriorates quickly below 0.5″ or so, with low sensitivity to objects with angular separations of 0.1″ or less on sky.

Background or foreground contaminant. With this in mind, we used the Besançon galactic model[8] to generate a representative star field around the position of LTT 9779, with the aim of testing the likelihood of having a diluted star that substantially affects the transit parameters. The model has been used in a similar manner previously. For instance, in ref. [37] they applied the model to test the probability that each of the Kepler transit planet candidates in their study was the result of a blended eclipsing binary. We selected all stars within a one square degree box surrounding our target, down to the magnitude limit of $V=21$ that the model provides. This gave rise to over 2,200 stars to work with, for which we randomly assign positions in right ascension and declination using a uniform random number generator, constrained to be within the selected box boundaries. We then ran the simulation ten million times to generate a representative sample, recording all the events where a star passed within a separation of 0.1″ from LTT 9779, and finally normalizing by the number of samples probed. The test returned only 48 events, providing a probability to have such a close separation between two stars in this field of only 4.8×10^{-6} (0.0005%).

Although the probability we found is very small, it is actually an upper limit. Blending by stars as faint as 21st magnitude, for instance, does not affect the transit depth enough to push the radius of the planet above the Neptune desert. The faintest population of stars in our test, which also represents the most abundant population, biases the probability to larger values. For instance, if we take the mean of the final bin (20.5 mag), we have a magnitude difference from LTT 9779 of 10.2, which relates to an effect at the level of 83 ppm, only 5% of the observed transit depth. If LTT 9779 b is truly a hot Jupiter, then to push it out of the Neptune desert, given its orbital period and current radius, we require dilution from a star of ~5.5 mag or brighter, limiting our test to only stars in magnitude bins of 16 or less. Performing this test decreases further the probability down to 1×10^{-6} (0.00001%), ruling out the possibility that dilution of the lightcurves is the reason the planet falls in such an isolated part of the parameter space.

Binary star contaminant. Although a non-bound stellar contaminant is unlikely to be diluting the transit of LTT 9779 b sufficiently to push it out of the Neptune desert, a binary companion is likely to have a higher chance to be present and tightly separated to LTT 9779. Therefore, we performed Monte Carlo simulations to test how likely having a stellar binary that is bright enough to dilute the transit lightcurve sufficiently would be. We simulated 10^5 binary systems, drawing the system parameters from the probability density functions (PDFs) calculated in ref. [38]. Here the orbital log-period PDF in days is a normal distribution with mean of 5.03 and standard deviation of 2.28. Most other parameters such as eccentricity, the orbital angles and the mass ratio, were simulated using uniform distributions within their respective bounds. Only the system inclinations were drawn from a cosine PDF.

When simulating the systems, we normalized each by the fraction of the orbital period that the secondary star would spend within 0.1″ of the primary. Therefore, systems that never approached within this angular separation were assigned a fractional time (T_f) of zero, those that always were found within this limit were assigned a value of unity, and the rest were assigned a value between 0 and 1 depending on the fractional time spent within this distance. With these calculations, we could apply the formulism $P=(\sum_{n=1}^{n=N_t} P_n T_{f,n})/N_t$, where the probability P is the sum total of fractional probabilities $P_n T_{f,n}$ across all samples n, normalized by the total number of samples N_t. Finally, we then normalized by the 46% fraction of such stars found to exist in binaries.

With these simulations we arrived at a value of 13.5% for the probability that LTT 9779 has a binary companion that could be found within an angular separation of 0.1″ at any one time. Although this is a relatively large probability, this is integrated across all binary mass fractions, and therefore does not take into account that only a small mass range is permitted by the spectral analysis. When we account for the cross-correlation function (CCF) analysis discussed below, the probability drops to essentially zero, as the larger secondary masses required to affect the transit depth sufficiently are all ruled out.

Gaia variability. Another way to probe for very closely separated stars on the sky is to study the measurements made by Gaia, in particular the excess noise parameter ϵ and the Tycho–Gaia astrometric solution (TGAS) discrepancy factor ΔQ (refs. [39–41]). These can be used to look for excess variability in the observations that are indicative of blended starlight from a foreground or background star, spatially close enough that they cannot be resolved by the instrument.

Both the ϵ and ΔQ parameters are listed in Gaia data release 1 (DR1) as standard outputs; however, Gaia DR2 reports only the excess noise, which turns out to be unreliable for stars with magnitudes $G<\sim13$ (ref. [42]). ΔQ measures the difference between the proper motion derived in TGAS and the proper motion derived in the Hipparcos Catalog[43]. Also, ref. [44] utilized both ΔQ and ϵ to show the lack of binarity for some stars. ΔQ is expected to follow a χ^2 distribution with two degrees of freedom for single stars. The Gaia DR1 ϵ and ΔQ for LTT 9779 are 0.394 (with a significance of 134.281) and 2.062, respectively. According to ref. [41], all sources obtain a significant excess source noise of ~0.5 mas, due to poor attitude modelling (so an excess noise >1–2 could indicate binarity), and a significance >2 indicates that the reported excess noise is significant; therefore, from excess noise alone, LTT 9779 is astrometrically well behaved and shows no evidence of binarity. While ref. [40] reports a ΔQ threshold of 15.086 for a star to be well behaved (at a significance level of 1%), ref. [41] reduces this threshold to 10. This means that any star with $\Delta Q<10$ is considered to be astrometrically well behaved, again showing that this star is highly likely to be uninfluenced by contaminating light from a background object.

Follow-up spectroscopy. *NRES spectroscopy.* To aid in characterization of the host star, we used the LCO robotic network of telescopes[45] and the NRES[11]. We obtained 3 spectra, each composed of $3\times1{,}200$ s exposures, on 5, 8 and 9 November 2018 UT. All three spectra were obtained with the Las Campanas Observatory (LCO)/NRES instrument mounted on a 1 m telescope at the LCO Cerro Tololo Inter-American Observatory node. The data were reduced using the LCO pipeline resulting in spectra with SNR of 61–73. We have analysed the spectra using SpecMatch while incorporating the Gaia DR2 parallax using the method described by ref. [46]. The resulting host stars parameters contributed to those listed in Supplementary Table 1.

TRES spectroscopy. We obtained two reconnaissance spectra on the nights of 4 and 5 November 2018 UT using the TRES[10] located at the Fred Lawrence Whipple Observatory in Arizona, USA. TRES has a resolving power of ~44,000, covering a wavelength range of 3,900–9,100 Å, and the resulting spectra were obtained with SNRs of ~35 at 5,200 Å. The spectra were then reduced and extracted as described in ref. [47], whereby the standard processing for echelle spectra of bias subtraction, cosmic ray removal, order-tracing, flatfielding, optimal extraction[48], blaze removal, scattered-light subtraction and wavelength calibration was applied. The Spectral Parameter Classification (SPC) tool[49] was used to measure the stellar quantities we show in Supplementary Table 1.

HARPS spectroscopy. On examination of the lightcurve, we decided to perform high-cadence follow-up spectroscopic observations with the HARPS[9] installed at the ESO 3.6 m telescope in La Silla, to fully cover the phase space. We started observing LTT 9779 on 6 November 2018. From an initial visual examination of the spectra and CCF of the online data reduction software, it was consistent with no evidence of blending with other stellar sources nor as being a fast rotator or active, based on the width of the CCF and various activity indicators.

We acquired 32 high-resolution ($R\approx115{,}000$) spectroscopic observations between 6 and 9 November, 11 to 13 December, and 28 to 30 December 2018, where for the nights of 7–9 November we observed the star four times throughout the night to fully sample the orbital period. We integrated for 1,200 s, using a simultaneous thorium–argon lamp comparison source feeding fibre B, and we achieved a mean SNR of ~65.4. We then reprocessed the observations using the HARPS-TERRA analysis software[50] where a high-signal-to-noise template is constructed from all the observed spectra. Then the radial velocities are computed by matching each individual observation to the template, and we list these measurements in Supplementary Table 2.

HARPS-TERRA receives the observed spectra, stellar coordinates, proper motions and parallaxes as input parameters. The output it produces then consists of a series of radial velocities that are calculated for a given wavelength range in the echelle. We used the weighted radial velocities that were calculated starting from the 25th order of the HARPS echellogram, which is centered at a wavelength of 4,500 Å. We chose this wavelength range as the uncertainties it produced had the lowest median absolute deviation value (where the median absolute deviation is equal to median(x_i − median(x)), with x representing the radial velocity of the ith order). This is likely due to increased stellar activity noise that affects the bluest orders the most, combined with relatively low SNRs, and therefore removing these orders allows higher precision to be reached. It was with this data that we

performed the EMPEROR (P. A. Peña-Rojas and J. S. Jenkins, manuscript in preparation) fitting, providing the independently confirmed and constrained evidence for LTT 9779 b (Extended Data Fig. 2). For instance, the Doppler orbital period was found to be 0.7920 ± 0.0001 d, in excellent agreement with that provided by the TESS transit fitting, and allowing the period to be constrained in the joint fit to 1 part in 80,000 (0.001%). We also used this spectra to test whether possible spectral line asymmetries and/or activity related features could be driving the signal. In particular, we searched for linear correlations between the spectral bisector inverse slope (BIS) measurements and the radial velocities (Extended Data Fig. 3), along with performing period searches using generalized Lomb–Scargle periodograms[51] and Bayesian methods with the EMPEROR code. The Spearman correlation coefficient between the BIS and radial velocities is found to be 0.22 with a P value of 0.22, meaning that there is no strong statistical evidence to reject the null hypothesis that such a weak correlation has arisen by chance. From the periodogram analyses, no statistically significant periodicities were detected with false alarm probabilities of less than 0.1%, our threshold for signal detection. We also performed the same analyses on the full-width at half-maximum (FWHM) of the HARPS CCF, and chromospheric activity indicators like the calcium HK S, Hα and He I indices, again with no statistically significant results encountered.

Finally, we also reprocessed the HARPS spectra to generate CCFs with binary masks optimized for spectral types between G2 and M4, but across a wider $\pm 200\,\mathrm{km\,s^{-1}}$ range in velocity to check for weaker secondary CCFs that could be due to additional, nearby companions. We took a typical HARPS LTT 9779 spectrum and injected mid-to-late M-star spectra with decreasing SNRs, until we could no longer detect the M-star CCFs, providing an upper limit on the mass of any contaminating secondary. From analysis of the mean flux ratio between the M stars and LTT 9779, we found that we should be able to detect stellar contaminants down to a mass of $0.19\,M_{\odot}$, using the mass–luminosity relation of ref. [52]; however, no companion CCFs were detected. Such a companion would have a magnitude difference of over 7.5, and as we previously calculated above that a maximum magnitude difference of 5.5 would be required to push LTT 9779 b out of the Neptune desert, the limits permitted by the CCF analysis show that a diluted companion would not change the conclusions of our work.

Coralie spectroscopy. Additional phase coverage was performed using the Coralie spectrograph installed in the 1.2 m Swiss Leonhard Euler Telescope at the ESO La Silla Observatory in Chile. Coralie has a spectral resolution of ~60,000 and uses a simultaneous calibration fibre illuminated by a Fabry–Perot etalon for correcting the instrumental radial-velocity drift that occurs during the science exposures. The star was observed a total of 18 times throughout the nights of 15–20 November 2018. The adopted exposure time for the Coralie observations was 1,200 s, and the SNR obtained per resolution element at 5,150 Å ranged between 50 and 60. Coralie data were processed with the CERES pipeline[53], which performs the optimal extraction of the science and calibration fibres, the wavelength calibration and instrumental drift correction, along with the measurement of precision radial velocities and bisector spans by using the cross-correlation technique. Specifically, a binary mask optimized for a G2-type star was used to compute the velocities for LTT 9779. The typical velocity precision achieved was $\sim 5\,\mathrm{m\,s^{-1}}$, which allowed the identification the Keplerian signal with an amplitude of 20^{-1}.

Follow-up high-angular resolution imaging. *NIRC2 at Keck.* As part of our standard process for validating transiting exoplanets, we observed LTT 9779 with infrared high-resolution adaptive optics imaging at the Keck Observatory[54]. The Keck Observatory observations were made with the NIRC2 instrument on Keck-II behind the natural guide star adaptive optics system. The observations were made on 22 November 2018 UT following the standard three-point dither pattern that is used with NIRC2 to avoid the left lower quadrant of the detector, which is typically noisier than the other three quadrants. The dither pattern step size was 3″ and was repeated twice, with each dither offset from the previous one by 0.5″.

The observations were made in the narrow-band Br−γ filter ($\lambda_0 = 2.1686$; $\Delta\lambda = 0.0326\,\mu$m) with an integration time of 2 s with one coadd per frame for a total of 18 s on target. The camera was in the narrow-angle mode with a full field of view of ~10″ and a pixel scale of approximately 0.0099442″ per pixel. The Keck adaptive optics observations show no additional stellar companions were detected to within a resolution ~0.056″ FWHM (Extended Data Fig. 4, left).

The sensitivities of the final combined adaptive optics image were determined by injecting simulated sources azimuthally around the primary target every 45° at separations of integer multiples of the central source's FWHM[55]. The brightness of each injected source was scaled until standard aperture photometry detected it with 5σ significance. The resulting brightness of the injected sources relative to the target set the contrast limits at that injection location. The final 5σ limit at each separation was determined from the average of all of the determined limits at that separation and the uncertainty on the limit was set by the RMS dispersion of the azimuthal slices at a given radial distance. The sensitivity curve is shown in the left panel of Extended Data Fig. 4, along with an inset image zoomed to primary target showing no other companion stars.

HRCam at SOAR. In addition to the Keck observations, we also searched for nearby sources to LTT 9779 with SOAR speckle imaging on 21 December 2018 UT, using the HRCam imager. Observations were performed in the I band, which is a similar visible bandpass to that of TESS. Observations consisted of 400 frames, consisting of a 200 × 200 binned pixels region of interest, centred on the star. Each individual frame is 6.3″ on a side, with a pixel scale of 0.01575″ and 2 × 2 binning, with an observation time of ~11 s and using an Andor iXon-888 camera. More details of the observations and processing are available in ref. [56].

The 5σ contrast curve and speckle autocorrelation function image are shown in the right panel of Extended Data Fig. 4. No nearby sources were detected within 3 of LTT 9779, down to a contrast limit of 6−7 mag in the I band. We can also rule out brighter background blends very close to the star, down to around 0.1″ separation. Combining the results from Keck and SOAR, we can rule out background blended eclipsing binaries contaminating the TESS large aperture used to build the LTT 9779 lightcurve.

Stellar parameters. To calculate the stellar parameters for LTT 9779, we used four different methods, with three of them applied to the three different sets of spectra we obtained from NRES, TRES and HARPS, and a photometric method that used our new tool ARIADNE. For the NRES spectra, we used the combination of SpecMatch and Gaia DR2 to perform the spectral classification, following the procedures explained in ref. [46]. TRES spectral observations used the SPC[49] tool to calculate the stellar parameters, whereas we used the Spectroscopic Parameters and Atmospheric Chemistries of Stars (SPECIES[57]) and the Zonal Atmospheric Stellar Parameters Estimator (ZASPE[58]) algorithms to analyse the HARPS spectra. Details of these methods can be found in each of the listed publications, yet in brief, SPC and ZASPE calculate the parameters by comparing the spectra to Kurucz synthetic model grids[59], either by direct spectral fitting or by cross-correlation. In this way, regions of the spectra that are sensitive to changes in stellar parameters can allow parameters to be estimated by searching for the best matching spectral model.

In contrast, SPECIES uses an automatic approach to calculate equivalent widths for large numbers of atomic spectral lines of interest, Fe I, for instance. The code then calculates the radiative transfer equation using MOOG[60], applying ATLAS9 model atmospheres[61], and converges on the stellar parameters using an iterative line rejection procedure. Convergence is reached once the constraints of having no statistical trend between abundances calculated from Fe I and Fe II, for example, reaches a pre-determined threshold value.

Each of these three methods return consistent results for the majority of the bulk parameters, in particular the stellar effective temperature is in excellent agreement, with a mean value of $5{,}480 \pm 42$ K, along with the surface gravity ($\log g$) of the star, which is found to be 4.47 ± 0.11 dex. For the metallicity of the star, all three methods find the star to be metal rich, with a mean value of $+0.27 \pm 0.04$ dex. For the main parameters of interest in this work, the stellar mass and radius, we used two different methods, with the mass value coming from the combination of the Gaia DR2 parallax for the star[5,6], along with either the MESA Isochrones and Stellar Tracks[62] models or the Yonsei–Yale[63] isochrones, and we find a value of $1.02^{+0.02}_{-0.03}\,M_{\odot}$.

For the radius, we used the ARIADNE code (J. I. Vines and J. S. Jenkins, manuscript in preparation), which is a new Python tool designed to automatically fit stellar spectral energy distributions in a Bayesian model averaging framework. We convolved Phoenix v2[64], BT-Settl, BT-Cond[65], BT-NextGen[65,66], ref. [61] and ref. [67] model grids with commonly available filter bandpasses—UBVRI; 2MASS JHK$_s$; SDSS ugriz; ALL-WISE W1 and W2; Gaia G, RP, and BP; Pan-STARRS griwyz; Stromgren uvby; GALEX NUV and FUV; Spitzer/IRAC 3.6 μm and 4.5 μm; TESS; Kepler; and NGTS—creating six different model grids, which we then interpolated in effective temperature $T_{\rm eff}$–$\log g$–[Fe/H] space. ARIADNE also fits for the radius, distance, extinction (Av) and excess noise terms for each photometry point used, to account for possible underestimated uncertainties. We used the SPECIES results as priors for the $T_{\rm eff}$, $\log g$ and [Fe/H], and the distance is constrained by the Gaia DR2 parallax, after correcting it by the offset found by ref. [68]. The radius has a prior based on Gaia's radius estimate and the Av has a flat prior limited to 0.029, as per the re-calibrated Schlegel, Finkbeiner and Davis galaxy dust map[69,70]. We performed the fit using dynesty's nested sampler[71], which returns the Bayesian evidence of each model, and then afterwards we averaged each model posterior samples weighted by their respective normalized evidence. This returned a final stellar radius of $0.949 \pm 0.006\,R_{\odot}$.

As LTT 9779 b appears as an odd-ball when scrutinizing its mass and radius, we want to be sure that the stellar radius is not biased in the sense that the star is really an evolved star, much larger than the stellar modelling predicts, and hence the planet is more likely an ultrahot Jupiter (UHJ). Although we have arrived at the same values from three different analyses and instrumental datasets, we can add more confidence to the results by studying the stellar density throughout the Markov chain Monte Carlo modelling process, when assuming the planet's orbit is circular. In this case, we place a log-uniform prior on the stellar density, constrained to be within $100–10{,}000\,\mathrm{kg\,m^{-3}}$, and then study how it changes as a function of the planet-to-star radius ratio $R_{\rm p}/R_{\rm .}$.

We find that the distribution is bimodal (Extended Data Fig. 5), with the most likely stellar density region given by the lower, more densely constrained part of the parameter space in the figure. The upper mode in the figure, pushing towards higher stellar densities and lower values of $R_{\rm p}/R_{\rm .}$, is arguing towards the star being an M dwarf, which is ruled out by the high-resolution spectroscopic data, and is

inconsistent with our global modelling effort (less probable part of the posterior space). This mode is also only consistent with a very narrow set of limb-darkening coefficients, all of which are inconsistent at several sigma with theoretical models, whereas the lower, more probable mode, has a wide range of possible limb-darkening coefficients, which are all in agreement with theoretical models. Therefore, this test rules out a more evolved state for the star in either case, with the higher probability mode being in excellent agreement with the results from the stellar modelling.

Finally, for the confirmation of the transit and radial-velocity parameters, it is prudent to analyse the activity of the star, to assess the impact that any activity could have on the measurements. From the above analyses we find the star to be a very slow rotator, with a HARPS $v\sin i$ limit of $1.06 \pm 0.37\,\mathrm{km\,s^{-1}}$, (where v is the measured rotational velocity and i the inclination of the rotation axis to our line of sight), which is lower than the projected solar $v\sin i$ value ($1.6 \pm 0.3\,\mathrm{km\,s^{-1}}$) determined from HARPS spectral analysis[72], indicating a slowly rotating and therefore inactive star. Given the calculated radius of the star, such a slow rotation gives rise to an upper limit of the rotation period to be 45 d. If the planetary orbit is aligned with the stellar plane of rotation, such that we can assume the inclination angle is the same, then this value is the absolute rotation period. Kepler Space Telescope data analysis of old field stars of this spectral type shows rotation periods ranging from a few days for the youngest stars, with a peak around 20 d, and a sharp fall after this with a tail reaching up to almost 100 d (ref. [73]). A rotation period of 45 d would place LTT 9779 in the upper tail of the Kepler distribution, indicating that the star is old, and agreeing with the combined age estimate of $2.0^{+1.3}_{-0.9}$ Gyr. This result would also suggest that the activity of the star should be weak. We calculate the activity using the Ca II HK lines, following the analysis procedures and methods presented in refs. [74–77]. We find the star to be inactive, with a HARPS S index of 0.148 ± 0.008, which relates to a mean $\log R'_{\mathrm{HK,HARPS}}$ of -5.10 ± 0.04 dex. Gyrochronology relations[78] would therefore suggest an age closer to ~5 Gyr or so, again confirming that the star should not be young. Taken all together, LTT 9779 can be classed as an inactive and metal-rich solar analogue star, and all key properties can be found in Supplementary Table 1.

Global modelling. As stated in the main text, the global modelling of the data was performed using juliet[12]. This code uses batman[79] to model the transit lightcurves and radvel[80] to model the radial velocities. We performed the posterior sampling using MultiNest[81] via the PyMultiNest wrapper[82].

The fit was parameterized by the parameters r_1 and r_2, both having uniform distributions between 0 and 1, which are transformations of the planet-to-star radius ratio p and impact parameter b that allow an efficient exploration of the parameter space[83]. In addition, we fitted for the stellar density by assuming a prior given by the value obtained with our analysis of the stellar properties, assuming a normal prior for this parameter with a mean of $1{,}810\,\mathrm{kg\,m^{-3}}$ and standard deviation of $130\,\mathrm{kg\,m^{-3}}$. We parameterized the limb-darkening effect using a quadratic law defined by parameters u_1 and u_2; however, we use an uninformative parameterization scheme[84] in which we fit for $q_1 = (u_1 + u_2)^2$ and $q_2 = u_1/(2u_1 + 2u_2)$ with q_1 and q_2 having uniform priors between 0 and 1. For the radial-velocity parameters, we used wide priors for both the systemic radial velocity of each instrument and the possible jitter terms, added in quadrature to the data.

For the photometry, we considered unitary dilution factors for the TESS NGTS and Las Cumbres Observatory Global Telescope (LCOGT) photometry after leaving them as free parameters and observing that it was not needed based on the posterior evidence of the fits. This is consistent with the a priori knowledge that the only source detected by Gaia DR2 within the TESS aperture is a couple of faint sources to the southeast of the target, the brighter of which has $\Delta G = 5.4$ with the target. If we assume the Gaia passband to be similar to the TESS passband, this would imply a dilution factor $D > 0.99$, which is negligible for our purposes. For the TESS photometry, no extra noise model nor jitter term was needed to be added according to the Bayesian evidence of fits incorporating those extra terms. For the NGTS observations, we considered the data of the target from the nine different telescopes as independent photometric datasets (that is, having independent out-of-transit baseline fluxes in the joint fit) that share the same limb-darkening coefficients. We initially added photometric jitter terms to all the NGTS observations, but found that fits without them for all instruments were preferred by looking at the Bayesian evidences of both fits. For the LCOGT data, we used Gaussian process in time to detrend a smooth trend observed in the data. A kernel that was a product of an exponential and a matern 3/2 was used, and a jitter term was also fitted and added in quadrature to the reported uncertainties in the data—this was the model that showed the largest Bayesian evidence. We note that fitting the lightcurves independently provides statistically similar transit depths to the joint model, showing that all are in statistical agreement. Finally, an eccentric orbit is ruled out by our data with an odds ratio of 49:1 in favour of a circular orbit; the eccentric fit, performed by parameterizing the eccentricity and argument of periastron via $\mathcal{S}_1 = \sqrt{e}\cos\omega$ and $\mathcal{S}_2 = \sqrt{e}\sin\omega$, (where ω is the argument of periastron passage), gives an eccentricity given our data of $e < 0.058$ with a 95% credibility.

With all the photometry in hand, we could also compare individually each lightcurve transit model to test whether they are in statistical agreement, or any biases exist, such that the radius measurement is biased. We proceeded to again fit each lightcurve independently with juliet, recording the transit model depths to test for statistical differences. As expected, we found the TESS photometry produced the most precise value ($T_{\mathrm{d,TESS}} = 2{,}299^{+320}_{-240}$ ppm), with the LCO and NGTS fits arriving at values of $T_{\mathrm{d,LCO}} = 1{,}925^{+620}_{-400}$ ppm and $1{,}594^{+980}_{-715}$ ppm, respectively. All three are in statistical agreement. We also jointly modelled the LCO and NGTS lightcurves to provide a more constrained comparison with the TESS photometry, and found a value of $T_{\mathrm{d,LCO+NGTS}} = 1{,}678^{+540}_{-290}$ ppm, again in statistical agreement with the TESS value. Therefore, we can be confident that all three instruments provide a similar description for the planet's physical size.

Transit timing variations. The transit timing variations (TTVs) of LTT 9779 b was measured using the EXOFASTv2[85,86] code. EXOFASTv2 uses the differential evolution Markov chain Monte Carlo method to derive the values and their uncertainties of the stellar, orbital and physical parameters of the system. For the TTV analysis of LTT 9779 b, we fixed the stellar and orbital parameters to the values obtained from the global fit performed by SPECIES and juliet, except for the transit time of each lightcurve and their baseline flux.

In a Keplerian orbit, the transit time of an exoplanet follows a linear function of the transit epoch number (E):

$$T_{\mathrm{c}}(E) = T_{\mathrm{c}}(0) + PE \quad (1)$$

where P is the orbital period of the exoplanet and $T_{\mathrm{c}}(0)$ is the optimal transit time in a arbitrary zero epoch and corresponds to the time that is least covariant with the period and has the smallest uncertainty. Our best-fitted value from EXOFASTv2 is: $T_{\mathrm{c}}(0) = 2{,}458{,}354.2145 \pm 0.0012$ barycentric Julian date.

All the transit times were allowed to move from the linear ephemeris and each one was considered as one independent TTV parameter in the EXOFASTv2's fitting, resulting in 33 parameters to fit. The best-fit results are shown in Extended Data Fig. 6, where the grey area corresponds to the 1σ of the linear ephemeris shown in equation (1).

We found no evidence of a clear periodic variation in the transit time. The RMS variation from the linear ephemeris is $\sigma = 181.8$ s. There are only two values above the 2σ limit; if we remove them, the RMS deviation is reduced to 155.9 s. However, the reduced chi-squared is $\chi^2_{\mathrm{red}} = 1.23$, which is an indicator that the transit times fit accordingly with the proposed linear ephemeris.

In conclusion, the existence of TTVs in LTT 9779 b is not evident for the time span of our transit data. In addition, with the apparent lack of another short-period signal in the radial-velocity data, this suggests that there is no other inner companion in the planetary system. Any other tertiary companion must be far from LTT 9779 b, such that the gravitation or tidal interactions are small, and the linear trend in the radial velocities might be pointing in that direction.

Metallicity analysis. The correlation between the presence of giant planets and host star metallicity has been well established[30,77,87,88], along with the apparent lack of any correlation for smaller planets[49,89,90]. We studied the small sample of known USP planets and UHJs (the gas giant planets with orbit periods of less than 1 d), using values taken from the TEPCat database[91], while recalculating metallicities for those where we could find their spectra (about half the sample) using SPECIES[57]. We found a similar general trend, whereby the USP planets tend to orbit more metal-poor stars when compared with the UHJs; however, the sample is small enough that single outliers bias the statistics, and we therefore extended slightly the orbital period selection out to 1.3 d, increasing the sample by over 55%. With this updated sample, we find a Kolmogorov–Smirnov test probability of only 1% that the USP planets and UHJs are drawn from the same parent population.

A couple of notable exceptions to the trend here are the planets 55 Cancri e and WASP-47 e, both small USP planets that orbit very metal-rich stars. However, there exists additional gas giant planets in these systems, meaning they still follow the overall picture. If we exclude these two, the Kolmogorov–Smirnov probability drops to 0.1% that the populations are statistically similar. The diversity of USP planets is high; therefore, many more detections are needed to statistically constrain the populations in this respect. We also require more UHJs to build up a statistical sample, since the subsolar metallicity of WASP-43 can also bias the tests. If we look at the density–metallicity parameter space (Fig. 4), there are indications of a general trend whereby the low-density planets are mostly UHJs orbiting metal-rich stars, and the higher-density USP planets orbit more metal-poor stars.

Data availability

The photometric data that support the findings of this study are publically available from the Mikulski Archive for Space Telescopes (http://archive.stsci.edu/) under the TESS mission link. All radial-velocity data are available from the corresponding author upon reasonable request. Raw and processed spectra can be obtained from the European Southern Observatory's data archive at http://archive.eso.org.

Code availability

All codes necessary for the reproduction of this work are publically available through the GitHub repository, as follows: EMPEROR, https://github.com/ReddTea/astroEMPEROR; Juliet, https://github.com/nespinoza/juliet; SPECIES, https://github.com/msotov/SPECIES ; ARIADNE, https://www.github.com/jvines/astroARIADNE.

Received: 9 July 2019; Accepted: 1 June 2020;
Published online: 14 September 2020

References

1. Sanchis-Ojeda, R. et al. A study of the shortest-period planets found with Kepler. *Astrophys. J.* **787**, 47 (2014).
2. Winn, J. N., Sanchis-Ojeda, R. & Rappaport, S. Kepler-78 and the ultra-short-period planets. *New Astron. Rev.* **83**, 37–48 (2018).
3. Ricker, G. R. et al. Transiting Exoplanet Survey Satellite (TESS). *J. Astron. Telesc. Instrum. Syst.* **1**, 014003 (2015).
4. Jenkins, J. M. et al. The TESS Science Processing Operations Center. *Proc. SPIE* **9913**, 99133E (2016).
5. Gaia Collaboration et al. The Gaia mission. *Astron. Astrophys.* **595**, A1 (2016).
6. Gaia Collaboration et al. Gaia data release 2. Summary of the contents and survey properties. *Astron. Astrophys.* **616**, A1 (2018).
7. Wheatley, P. J. et al. The Next Generation Transit Survey (NGTS). *Mon. Not. R. Astron. Soc.* **475**, 4476–4493 (2018).
8. Robin, A. C., Reylé, C., Derriére, S. & Picaud, S. A synthetic view on structure and evolution of the Milky Way. *Astron. Astrophys.* **409**, 523–540 (2003).
9. Pepe, F. et al. HARPS: a new high-resolution spectrograph for the search of extrasolar planets. *Proc. SPIE* **4008**, 582–592 (2000).
10. Fűrész, G., Szentgyorgyi, A. H. & Meibom, S. in *Precision Spectroscopy in Astrophysics* (eds Santos, N. C. et al.) 287–290 (Springer, 2008).
11. Siverd, R. J. et al. NRES: the network of robotic echelle spectrographs. *Proc. SPIE* **10702**, 107026C (2018).
12. Espinoza, N., Kossakowski, D. & Brahm, R. Juliet: a versatile modelling tool for transiting and non-transiting exoplanetary systems. *Mon. Not. R. Astron. Soc.* **490**, 2262–2283 (2019).
13. Mazeh, T., Holczer, T. & Faigler, S. Dearth of short-period neptunian exoplanets: a desert in period-mass and period-radius planes. *Astron. Astrophys.* **589**, A75 (2016).
14. Lopez, E. D. & Fortney, J. J. Understanding the mass-radius relation for sub-Neptunes: radius as a proxy for composition. *Astrophys. J.* **792**, 1 (2014).
15. Lundkvist, M. S. et al. Hot super-Earths stripped by their host stars. *Nat. Commun.* **7**, 11201 (2016).
16. Lopez, E. D. Born dry in the photoevaporation desert: Kepler's ultra-short-period planets formed water-poor. *Mon. Not. R. Astron. Soc.* **472**, 245–253 (2017).
17. Owen, J. E. & Wu, Y. The evaporation valley in the Kepler planets. *Astrophys. J.* **847**, 29 (2017).
18. Ehrenreich, D. et al. A giant comet-like cloud of hydrogen escaping the warm Neptune-mass exoplanet GJ 436b. *Nature* **522**, 459–461 (2015).
19. Vidal-Madjar, A. et al. Detection of oxygen and carbon in the hydrodynamically escaping atmosphere of the extrasolar planet HD 209458b. *Astrophys. J. Lett.* **604**, L69–L72 (2004).
20. Casasayas-Barris, N. et al. Atmospheric characterization of the ultra-hot Jupiter MASCARA-2b/KELT-20b. Detection of CaII, FeII, NaI, and the Balmer series of H (Hα, Hβ, and Hγ) with high-dispersion transit spectroscopy. *Astron. Astrophys.* **628**, 9 (2019).
21. Nortmann, L. et al. Ground-based detection of an extended helium atmosphere in the Saturn-mass exoplanet WASP-69b. *Science* **362**, 1388–1391 (2018).
22. West, R. G. et al. NGTS-4b: A sub-Neptune transiting in the desert. *Mon. Not. R. Astron. Soc.* **486**, 5094–5103 (2019).
23. Owen, A. E. & Jackson, A. P. Planetary evaporation by UV, X-ray radiation: basic hydrodynamics. *Mon. Not. R. Astron. Soc.* **425**, 2931–2947 (2012).
24. Ionov, D. E., Pavlyuchenkov, Y. N. & Shematovich, V. I. Survival of a planet in short-period Neptunian desert under effect of photoevaporation. *Mon. Not. R. Astron. Soc.* **476**, 5639–5644 (2018).
25. Jackson, A. P., Davis, T. A. & Wheatley, P. The coronal X-ray-age relation and its implications for the evaporation of exoplanets. *Mon. Not. R. Astron. Soc.* **422**, 2024–2043 (2012).
26. Chadney, J. M. et al. XUV-driven mass loss from extrasolar giant planets orbiting active stars. *Icarus* **250**, 357–367 (2015).
27. King, G. W. et al. The XUV environments of exoplanets from Jupiter-size to super-Earth. *Mon. Not. R. Astron. Soc.* **478**, 1193–1208 (2018).
28. Kubyshkina, D. et al. Grid of upper atmosphere models for 1–40 $M_{\oplus}$ planets: application to CoRoT-7 b and HD 219134 b,c. *Astron. Astrophys.* **619**, A151 (2018).
29. Valsecchi, F. et al. Tidally-driven Roche-lobe overflow of hot Jupiters with MESA. *Astrophys. J.* **813**, 101 (2015).
30. Fischer, D. A. & Valenti, J. The planet–metallicity correlation. *Astrophys. J.* **622**, 1102–1117 (2005).
31. Smith, J. C. et al. Kepler presearch data conditioning II—a Bayesian approach to systematic error correction. *Publ. Astron. Soc. Pac.* **124**, 1000–1014 (2012).
32. Stumpe, M. C. et al. Multiscale systematic error correction via wavelet-based bandsplitting in Kepler data. *Publ. Astron. Soc. Pac.* **126**, 100–114 (2014).
33. Twicken, J. D. et al. Kepler data validation I architecture, diagnostic tests,and data products for vetting transiting planet candidates. *Publ. Astron. Soc. Pac.* **130**, 064502 (2018).
34. Li, J. et al. Kepler data validation II—transit model fitting and multiple-planet search. *Publ. Astron. Soc. Pac.* **131**, 024506 (2019).
35. Smith, A. M. S. et al. Shallow transit follow-up from Next-Generation Transit Survey: simultaneous observations of HD106315 with 11 identical telescopes. *Astron. Nachr.* **341**, 273–282 (2020).
36. McCormac, J. et al. DONUTS: a science frame autoguiding algorithm with sub-pixel precision, capable of guiding on defocused stars. *Publ. Astron. Soc. Pac.* **125**, 548–556 (2013).
37. Fressin, F. et al. The false positive rate of Kepler and the occurrence of planets. *Astrophys. J.* **766**, 81 (2013).
38. Raghavan, D. et al. A survey of stellar families: multiplicity of solar-type stars. *Astrophys. J. Suppl. Ser.* **190**, 1–42 (2010).
39. Lindegren, L. et al. The astrometric core solution for the Gaia mission. Overview of models, algorithms, and software implementation. *Astron. Astrophys.* **538**, A78 (2012).
40. Michalik, D., Lindegren, L., Hobbs, D. & Lammers, U. Joint astrometric solution of HIPPARCOS and Gaia. A recipe for the hundred thousand proper motions project. *Astron. Astrophys.* **571**, A85 (2014).
41. Lindegren, L. et al. Gaia data release 1. Astrometry: one billion positions, two million proper motions and parallaxes. *Astron. Astrophys.* **595**, A4 (2016).
42. Lindegren, L. Gaia data release 2. The astrometric solution. *Astron. Astrophys.* **616**, A2 (2018).
43. van Leeuwen, F. Validation of the new Hipparcos reduction. *Astron. Astrophys.* **474**, 653–664 (2007).
44. Rey, J. et al. The SOPHIE search for northern extrasolar planets. XII. Three giant planets suitable for astrometric mass determination with Gaia. *Astron. Astrophys.* **601**, A9 (2017).
45. Brown, T. M. et al. Las Cumbres Observatory Global Telescope Network. *Publ. Astron. Soc. Pac.* **125**, 1031 (2013).
46. Fulton, B. J. & Petigura, E. A. The California–Kepler Survey. VII. Precise planet radii leveraging Gaia DR2 reveal the stellar mass dependence of the planet radius gap. *Astron. J.* **156**, 264 (2018).
47. Buchhave, L. A. et al. HAT-P-16b: A 4 $M_{\rm J}$ planet transiting a bright star on an eccentric orbit. *Astrophys. J.* **720**, 1118–1125 (2010).
48. Horne, K. An optimal extraction algorithm for CCD spectroscopy. *Publ. Astron. Soc. Pac.* **98**, 609–617 (1986).
49. Buchhave, L. A. et al. An abundance of small exoplanets around stars with a wide range of metallicities. *Nature* **486**, 375–377 (2012).
50. Anglada-Escudé, G. & Butler, R. P. The HARPS-TERRA project. I. Description of the algorithms, performance, and new measurements on a few remarkable stars observed by HARPS. *Astrophys. J. Suppl. Ser.* **200**, 15 (2012).
51. Zechmeister, M. & Kürster, M. The generalised Lomb–Scargle periodogram. A new formalism for the floating-mean and Keplerian periodograms. *Astron. Astrophys.* **496**, 577–584 (1986).
52. Benedict, G. F. et al. The solar neighborhood. XXXVII: the mass–luminosity relation for main-sequence M dwarfs. *Astron. J.* **152**, 141 (2016).
53. Brahm, R., Jordán, A. & Espinoza, N. CERES: a set of automated routines for echelle spectra. *Publ. Astron. Soc. Pac.* **129**, 034002 (2017).
54. Ciardi, D. R., Beichman, C. A., Horch, E. P. & Howell, S. B. Understanding the effects of stellar multiplicity on the derived planet radii from transit surveys: implications for Kepler, K2, and TESS. *Astrophys. J.* **805**, 16 (2015).
55. Furlan, E. et al. The Kepler follow-up observation program. I. A catalog of companions to Kepler stars from high-resolution imaging. *Astron. J.* **153**, 71 (2017).
56. Ziegler, C. et al. SOAR TESS survey. I: sculpting of tess planetary systems by stellar companions. *Astron. J.* **159**, 19 (2020).
57. Soto, M. G. & Jenkins, J. S. Spectroscopic parameters and atmospheric chemistries of stars (SPECIES). I. Code description and dwarf stars catalogue. *Astron. Astrophys.* **615**, A76 (2018).
58. Brahm, R., Jordán, A., Hartman, J. & Bakos, G. ZASPE: A code to measure stellar atmospheric parameters and their covariance from spectra. *Mon. Not. R. Astron. Soc.* **467**, 971–984 (2017).
59. Kurucz, R. L. in *The Stellar Populations of Galaxies* IAU Symposium Vol. 149 (eds Barbuy, B. & Renzini, A.) 225 (1992).
60. Sneden, C. A. *Carbon and Nitrogen Abundances in Metal-Poor Stars.* PhD thesis, Univ. Texas at Austin (1973).
61. Castelli, F. & Kurucz, R. L. New grids of ATLAS9 model atmospheres. In *Symposium of the International Astronomical Union* A20 (Astronomical Society of the Pacific, 2003).
62. Dotter, A. MESA isochrones and stellar tracks (MIST) 0: methods for the construction of stellar isochrones. *Astrophys. J. Suppl. Ser.* **222**, 8 (2016).
63. Yi, S. et al. Toward better age estimates for stellar populations: the Y2 isochrones for solar mixture. *Astrophys. J. Suppl. Ser.* **136**, 417–437 (2001).
64. Husser, T. O. et al. A new extensive library of PHOENIX stellar atmospheres and synthetic spectra. *Astron. Astrophys.* **553**, A6 (2013).

65. Allard, F., Homeier, D. & Freytag, B. Models of very-low-mass stars, brown dwarfs and exoplanets. *Phil. Trans. R. Soc. Lond. Ser. A* **379**, 2765–2777 (2012).
66. Hauschildt, P. H., Allard, F. & Baron, E. The NextGen Model Atmosphere grid for $3000 \leq T_{\rm eff} \leq 10{,}000$ K. *Astrophys. J.* **512**, 377–385 (1999).
67. Kurucz, R. et al. *ATLAS9 Stellar Atmosphere Programs and 2 km/s Grid* Kurucz CD-ROM No. 13 (Smithsonian Astrophysical Observatory, 1993).
68. Stassun, K. G. & Torres, G. Evidence for a systematic offset of 80 micro-arcseconds in the Gaia DR2 parallaxes. *Astron. J.* **862**, 1–5 (2018).
69. Schlegel, D. J., Finkbeiner, D. P. & Davis, M. Maps of dust infrared emission for use in estimation of reddening and cosmic microwave background radiation foregrounds. *Astrophys. J.* **500**, 525–553 (1998).
70. Schlafly, E. F. & Finkbeiner, D. P. Measuring reddening with Sloan Digital Sky Survey stellar spectra and recalibrating SFD. *Astrophys. J.* **737**, 103 (2011).
71. Speagle, J. S. dynesty: a dynamic nested sampling package for estimating Bayesian posteriors and evidences. *Mon. Not. R. Astron. Soc.* **493**, 3132–3158 (2020).
72. Pavlenko, Y. V., Jenkins, J. S., Jones, H. R. A., Ivanyuk, O. & Pinfield, D. J. Effective temperatures, rotational velocities, microturbulent velocities and abundances in the atmospheres of the Sun, HD 1835 and HD 10700. *Mon. Not. R. Astron. Soc.* **422**, 542–552 (2012).
73. McQuillan, A., Mazeh, T. & Aigrain, S. Rotation periods of 34,030 Kepler main-sequence stars: the full autocorrelation sample. *Astrophys. J. Suppl. Ser.* **211**, 24 (2014).
74. Jenkins, J. S. et al. An activity catalogue of southern stars. *Mon. Not. R. Astron. Soc.* **372**, 163–173 (2006).
75. Jenkins, J. S. et al. Metallicities and activities of southern stars. *Astron. Astrophys.* **485**, 571–584 (2008).
76. Jenkins, J. S. et al. Chromospheric activities and kinematics for solar type dwarfs and subgiants: analysis of the activity distribution and the AVR. *Astron. Astrophys.* **531**, A8 (2011).
77. Jenkins, J. S. et al. New planetary systems from the Calan–Hertfordshire extrasolar planet search. *Mon. Not. R. Astron. Soc.* **466**, 443–473 (2017).
78. Mamajek, E. E. & Hillenbrand, L. A. Improved age estimation for solar-type dwarfs using activity-rotation diagnostics. *Astrophys. J.* **687**, 1264–1293 (2008).
79. Kreidberg, L. batman: basic transit model calculation in Python. *Publ. Astron. Soc. Pac.* **127**, 1161–1165 (2015).
80. Fulton, B. J., Petigura, E. A., Blunt, S. & Sinukoff, E. RadVel: the radial velocity modeling toolkit. *Publ. Astron. Soc. Pac.* **130**, 044504 (2018).
81. Feroz, F., Hobson, M. P. & Bridges, M. MULTINEST: an efficient and robust bayesian inference tool for cosmology and particle physics. *Mon. Not. R. Astron. Soc.* **398**, 1601–1614 (2009).
82. Buchner, J. et al. X-ray spectral modelling of the AGN obscuring region in the CDFS: Bayesian model selection and catalogue. *Astron. Astrophys.* **564**, A125 (2014).
83. Espinoza, N. Efficient joint sampling of impact parameters and transit depths in transiting exoplanet light curves. *Res. Not. Am. Astron. Soc.* **2**, 209 (2018).
84. Kipping, D. M. Efficient, uninformative sampling of limb darkening coefficients for two-parameter laws. *Mon. Not. R. Astron. Soc.* **435**, 2152–2162 (2013).
85. Eastman, J., Gaudi, B. S. & Algol, E. EXOFAST: A fast exoplanetary fitting suite in IDL. *Publ. Astron. Soc. Pac.* **125**, 83–112 (2013).
86. Eastman, J. EXOFASTv2: generalized publication-quality exoplanet modeling code. *Astrophys. Source Code Library* **435**, 1710.003 (2017).
87. Gonzalez, G. The stellar metallicity–giant planet connection. *Mon. Not. R. Astron. Soc.* **285**, 403–412 (1997).
88. Maldonado, J., Villaver, E. & Eiroa, C. Chemical fingerprints of hot Jupiter planet formation. *Astron. Astrophys.* **612**, A93 (2018).
89. Jenkins, J. S. et al. A hot Uranus orbiting the super metal-rich star HD 77338 and the metallicity–mass connection. *Astrophys. J.* **766**, 67 (2013).
90. Buchhave, L. et al. Three regimes of extrasolar planet radius inferred from host star metallicities. *Nature* **509**, 593–595 (2014).
91. Southworth, L. Homogeneous studies of transiting extrasolar planets—IV. Thirty systems with space-based light curves. *Mon. Not. R. Astron. Soc.* **417**, 2166–2196 (2011).
92. Méndez, A. & Rivera-Valentín, E. G. The equilibrium temperature of planets in elliptical orbits. *Astrophys. J. Lett.* **837**, L1 (2017).
93. Zeng, L., Sasselov, D. D. & Jacobsen, S. B. Mass–radius relation for rocky planets based on PREM. *Astrophys. J.* **819**, 127 (2016).

Acknowledgements

Funding for the TESS mission is provided by NASA's Science Mission directorate. We acknowledge the use of public TESS alert data from pipelines at the TESS Science Office and at the TESS Science Processing Operations Center. This research has made use of the Exoplanet Follow-up Observation Program website, which is operated by the California Institute of Technology, under contract with the National Aeronautics and Space Administration under the Exoplanet Exploration Program. Resources supporting this work were provided by the NASA High-End Computing (HEC) Program through the NASA Advanced Supercomputing (NAS) Division at Ames Research Center for the production of the SPOC data products. J.S.J. and N.T. acknowledge support by FONDECYT grants 1161218 and 1201371, and partial support from CONICYT project Basal AFB-170002. M.R.D. is supported by CONICYT-PFCHA/Doctorado Nacional-21140646/Chile and Proyecto Basal AFB-170002. J.I.V. acknowledges support of CONICYT-PFCHA/Doctorado Nacional-21191829. This work was made possible owing to ESO Projects 0102.C-0525 (principal investigator, Díaz) and 0102.C-0451 (principal investigator, Brahm). R.B. acknowledges support from FONDECYT Post-doctoral Fellowship Project 3180246. This work is partly supported by JSPS KAKENHI grant numbers JP18H01265 and JP18H05439, and JST PRESTO grant number JPMJPR1775. The IRSF project is a collaboration between Nagoya University and the South African Astronomical Observatory (SAAO) supported by the Grants-in-Aid for Scientific Research on Priority Areas (A) (numbers 10147207 and 10147214) and Optical and Near-Infrared Astronomy Inter-University Cooperation Program, from the Ministry of Education, Culture, Sports, Science and Technology (MEXT) of Japan and the National Research Foundation (NRF) of South Africa. We thank A. Fukui, N. Kusakabe, K. Morihana, T. Nagata, T. Nagayama and the staff of SAAO for their kind support for IRSF SIRIUS observations and analyses. C.P. acknowledges support from the Gruber Foundation Fellowship and Jeffrey L. Bishop Fellowship. This research includes data collected under the NGTS project at the ESO La Silla Paranal Observatory. NGTS is funded by a consortium of institutes consisting of the University of Warwick, the University of Leicester, Queen's University Belfast, the University of Geneva, the Deutsches Zentrum für Luft- und Raumfahrt e.V. (DLR; under the 'Großinvestition GI-NGTS'), the University of Cambridge, together with the UK Science and Technology Facilities Council (STFC; project reference ST/M001962/1 and ST/S002642/1). P.J.W., D.B., B.T.G., S.G., T.L., D.P. and R.G.W. are supported by STFC consolidated grant ST/P000495/1. D.J.A. gratefully acknowledges support from the STFC via an Ernest Rutherford Fellowship (ST/R00384X/1). E.G. gratefully acknowledges support from the David and Claudia Harding Foundation in the form of a Winton Exoplanet Fellowship. M.J.H. acknowledges funding from the Northern Ireland Department for the Economy. M.T. is supported by JSPS KAKENHI (18H05442, 15H02063). A.J., R.B. and P.T. acknowledge support from FONDECYT project 1171208, and by the Ministry for the Economy, Development, and Tourism's Programa Iniciativa Científica Milenio through grant IC 120009, awarded to the Millennium Institute of Astrophysics (MAS). P.E., A.C. and H.R. acknowledge the support of the DFG priority programme SPP 1992 'Exploring the Diversity of Extrasolar Planets' (RA 714/13-1). We acknowledge the effort of A. Tokovinin in helping to perform the observations and reduction of the SOAR data.

Author contributions

J.S.J. led the TESS precision radial-velocity follow-up programme, selection of the targets, analysis and project coordination, and wrote the bulk of the paper. M.D., N.T. and R.B. performed the HARPS radial-velocity observations, P.T. observed the star with Coralie and M.D. analysed the activity data from these sources. N.E. performed the global modelling, with P.C.-Z. performing the TTV analysis, and R.B., M.G.S. and A.B. performing the stellar characterization using the spectra and evolutionary models. P.A.P.R. worked on the EMPEROR code and assisted in fitting the HARPS radial velocities. E.D.L. created a structure model for the planet, and in addition to G.W.K. and P.J.W., performed photoevaporation modelling. J.N.W. performed analysis of the system parameters. D.R.C. led the Keck NIRC2 observations and analysis. G.R., R.V., D.W.L., S.S. and J.M.J. have been leading the TESS project, observations, organization of the mission, processing of the data, organization of the working groups, selection of the targets and dissemination of the data products. C.E.H., S.M. and T.K. worked on the SPOC data pipeline. C.J.B. was a member of the TOI discovery team. S.N.Q. contributed to TOI vetting, TFOP organization and TRES spectral analysis. J.L. and C.P. helped with the interpretation of the system formation and evolution. K.A.C. contributed to TOI vetting, TFOP organization, and TFOP SG1 ground-based time-series photometry analysis. G.I., F.M., A.E., K.I.C., M.M., N.N., T.N. and J.P.L. contributed TFOP SG1 observations. J.S.A., D.J.A., D.B., F.B., C.B., E.M.B., M.R.B., J.C., S.L.C., A.C., B.F.C., P.E., A.E., E.F., B.T.G., S.G., E.G., M.N.G., M.R.G., M.J.H., J.A.G.J., T.L., J.M., M.M., L.D.N., D.P., D.Q., H.R., L.R., A.M.S.S., R.H.T., R.T.-W., O.T., S.U., J.I.V., S.R.W., C.A.W., R.G.W., P.J.W. and G.W.K. are part of the NGTS consortium who provided follow-up observations to confirm the planet. E.P. and J.J.L. helped with the interpretation of the result. C.B. performed the observations at SOAR and reduced the data, C.Z. performed the data analysis, and N.L. and A.W.M. assisted in the survey proposal, analysis and telescope time acquisition. All authors contributed to the paper.

Competing interests

The authors declare no competing interests.

Additional information

Extended data is available for this paper at https://doi.org/10.1038/s41550-020-1142-z.

Supplementary information is available for this paper at https://doi.org/10.1038/s41550-020-1142-z.

Correspondence and requests for materials should be addressed to J.S.J.

Reprints and permissions information is available at www.nature.com/reprints.

Publisher's note Springer Nature remains neutral with regard to jurisdictional claims in published maps and institutional affiliations.

[1]Departamento de Astronomía, Universidad de Chile, Las Condes, Chile. [2]Centro de Astrofísica y Tecnologías Afines (CATA), Santiago, Chile. [3]Space Telescope Science Institute, Baltimore, MD, USA. [4]Center of Astro-Engineering UC, Pontificia Universidad Católica de Chile, Santiago, Chile. [5]Millennium Institute for Astrophysics, Santiago, Chile. [6]School of Physics and Astronomy, Queen Mary University of London, London, UK. [7]NASA Goddard Space Flight Center, Greenbelt, MD, USA. [8]Department of Physics, University of Warwick, Coventry, UK. [9]Centre for Exoplanets and Habitability, University of Warwick, Coventry, UK. [10]Department of Astrophysical Sciences, Princeton University, Princeton, NJ, USA. [11]NASA Exoplanet Science Institute, Caltech, Pasadena, CA, USA. [12]Department of Physics and Kavli Institute for Astrophysics and Space Research, Massachusetts Institute of Technology, Cambridge, MA, USA. [13]Royal Observatory of Belgium, Brussels, Belgium. [14]Center for Astrophysics | Harvard and Smithsonian, Cambridge, MA, USA. [15]Department of Earth and Planetary Sciences, Massachusetts Institute of Technology, Cambridge, MA, USA. [16]NASA Ames Research Center, Moffett Field, CA, USA. [17]Department of Astronomy, The University of Tokyo, Tokyo, Japan. [18]Komaba Institute for Science, The University of Tokyo, Tokyo, Japan. [19]PRESTO, JST, Tokyo, Japan. [20]Astrobiology Center, Tokyo, Japan. [21]National Astronomical Observatory of Japan, Tokyo, Japan. [22]Instituto de Astrofísica de Canarias (IAC), Tenerife, Spain. [23]Department of Physics, Kyoto Sangyo University, Kyoto, Japan. [24]George Mason University, Fairfax, VA, USA. [25]Campo Catino Astronomical Observatory, Guarcino, Italy. [26]Canadian Institute for Theoretical Astrophysics, University of Toronto, Toronto, Ontario, Canada. [27]Centre for Planetary Sciences, Department of Physical and Environmental Sciences, University of Toronto at Scarborough, Toronto, Ontario, Canada. [28]Facultad de Ingeniería y Ciencias, Universidad Adolfo Ibáñez, Peñalolén, Chile. [29]Department of Physics and Astronomy, University of Leicester, Leicester, UK. [30]Observatoire de Genéve, Université de Genéve, Sauverny, Switzerland. [31]Institute of Planetary Research, German Aerospace Center, Berlin, Germany. [32]Center for Astronomy and Astrophysics, TU Berlin, Berlin, Germany. [33]Astrophysics Group, Cavendish Laboratory, Cambridge, UK. [34]Astrophysics Research Centre, School of Mathematics and Physics, Queen's University Belfast, Belfast, UK. [35]Instituto de Astronomía, Universidad Católica del Norte, Antofagasta, Chile. [36]Institute of Geological Sciences, FU Berlin, Berlin, Germany. [37]Departamento de Astrofísica, Universidad de La Laguna (ULL), Tenerife, Spain. [38]Dunlap Institute for Astronomy and Astrophysics, University of Toronto, Toronto, Ontario, Canada. [39]Department of Physics and Astronomy, The University of North Carolina at Chapel Hill, Chapel Hill, NC, USA. [40]Present address: Facultad de Ingeniería y Ciencias, Universidad Adolfo Ibáñez, Peñalolén, Chile.
✉e-mail: jjenkins@das.uchile.cl

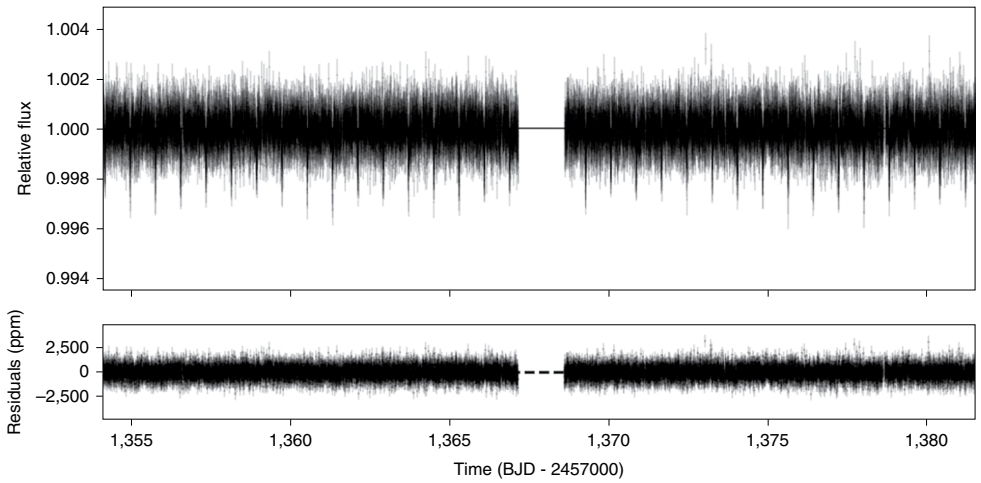

Extended Data Fig. 1 | Normalised TESS pre-search data conditioning timeseries photometry for LTT 9779. with the optimal model (black curve) overplotted on the data (top). The model residuals are shown in the lower panel.

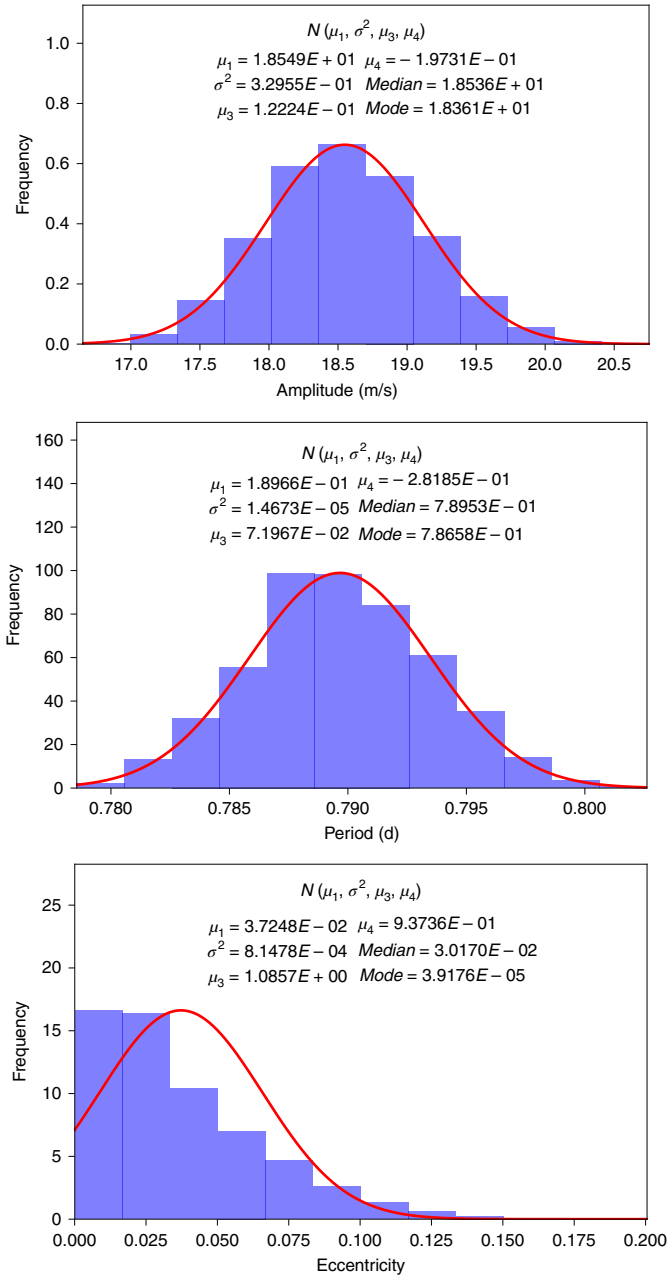

Extended Data Fig. 2 | Independently constrained system parameters from the EMPEROR MCMC runs of the 31 HARPS radial-velocities. From top to bottom we show the posteriors of the velocity amplitude, the orbital period, and the eccentricity of the orbit. Overplotted on each histogram is a gaussian distribution with the same input parameters as those calculated from the posterior distributions. We also show the values obtained from the distributions. The histograms reveal that the signal is well constrained with the current data in hand, and the period in particular is in excellent agreement with that from the TESS lightcurve.

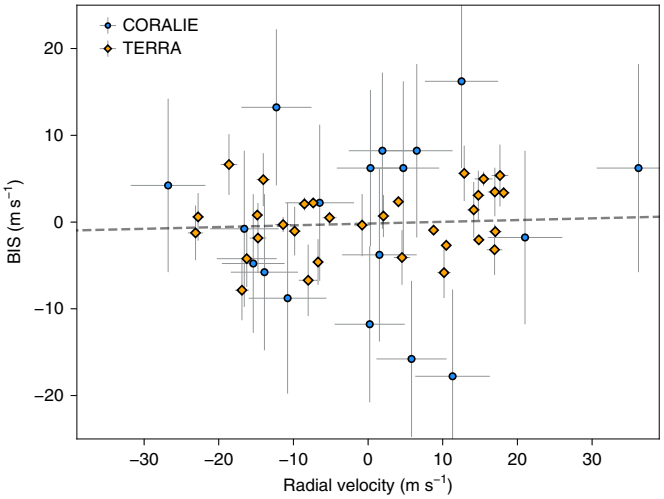

Extended Data Fig. 3 | Spectral line bisector inverse slope measurements as a function of the radial-velocities. The orange diamonds and blue circles relate to measurements made using HARPS and Coralie, respectively. The best fit linear trend is shown by the dashed line, and a key in the upper left indicates the origin of the data points.

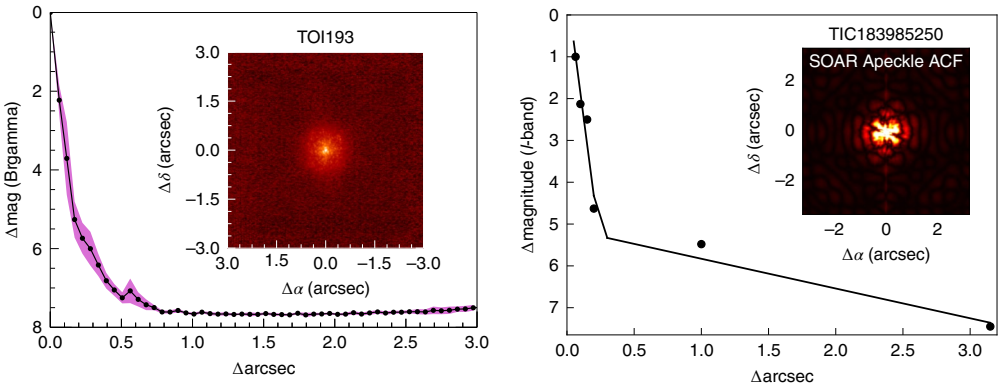

Extended Data Fig. 4 | Companion sensitivity for the Keck NIRC2 adaptive optics imaging and the SOAR Adaptive Optics Module (SAM). For NIRC2 (left), the black points represent the 5σ limits and are separated in steps of 1 FWHM (~ 0.05″); the purple represents the azimuthal dispersion (1σ) of the contrast determinations (see text). The inset image is of the primary target showing no additional companions within 3″ of the target. For SAM (right) the black curve also represents the 5σ limit, and the black data points mark the sampling. The inset also shows the speckle image of the star, constructed from the Auto-Correlation Function.

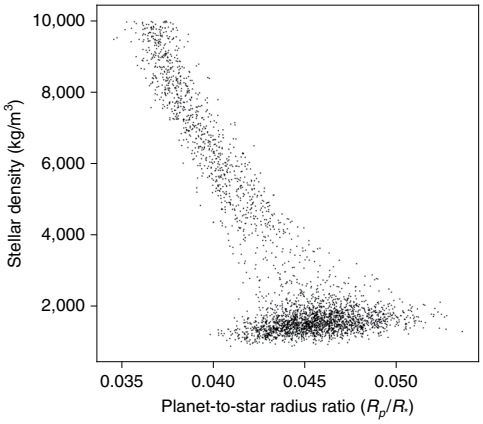

Extended Data Fig. 5 | Stellar density as a function of R_p/R*. when modelling the TESS, NGTS, and LCOGT lightcurves with a log-uniform prior on the stellar density and the planetary eccentricity constrained to be zero.

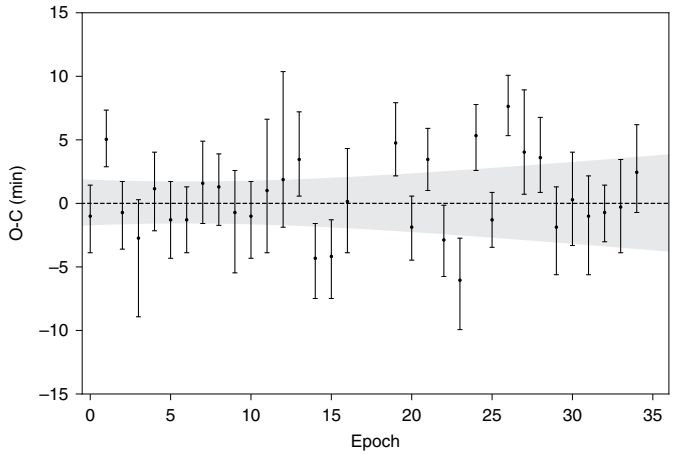

Extended Data Fig. 6 | Observed minus computed mid-transit times of LTT 9779 b. The residuals (TTV) of the transit times are shown considering the proposed linear ephemeris. The dashed line corresponds to zero variation and the grey area is the propagation of 1σ uncertainties, considering the optimal transit time from EXOFASTv2 and the period from juliet. The epoch 0 is the first lightcurve obtained by TESS and is also the corresponding epoch of the optimal transit time. The TTV values shown in this plot fit accordingly with the proposed linear ephemeris ($\chi^2_{red} = 1.23 = 1.23$).